

12-1-2022

Calcite Spherulite Formations and Their Controls in Halophilic Bacterial Cultures

Zakaria Jibrin

Follow this and additional works at: <https://digitalscholarship.unlv.edu/thesesdissertations>



Part of the [Microbiology Commons](#), and the [Mineral Physics Commons](#)

Repository Citation

Jibrin, Zakaria, "Calcite Spherulite Formations and Their Controls in Halophilic Bacterial Cultures" (2022). *UNLV Theses, Dissertations, Professional Papers, and Capstones*. 4593. <http://dx.doi.org/10.34917/35777475>

This Thesis is protected by copyright and/or related rights. It has been brought to you by Digital Scholarship@UNLV with permission from the rights-holder(s). You are free to use this Thesis in any way that is permitted by the copyright and related rights legislation that applies to your use. For other uses you need to obtain permission from the rights-holder(s) directly, unless additional rights are indicated by a Creative Commons license in the record and/or on the work itself.

This Thesis has been accepted for inclusion in UNLV Theses, Dissertations, Professional Papers, and Capstones by an authorized administrator of Digital Scholarship@UNLV. For more information, please contact digitalscholarship@unlv.edu.

CALCITE SPHERULITE FORMATIONS AND THEIR CONTROLS IN HALOPHILIC
BACTERIAL CULTURES

By

Zakaria Jibrin

Bachelor of Science - Geology
University of Arizona
2019

A thesis submitted in partial fulfillment
of the requirements for the

Master of Science – Geoscience

Department of Geoscience
College of Sciences
The Graduate College

University of Nevada, Las Vegas
December 2022



Thesis Approval

The Graduate College
The University of Nevada, Las Vegas

November 22, 2022

This thesis prepared by

Zakaria Jibrin

entitled

Calcite Spherulite Formations and Their Controls in Halophilic Bacterial Cultures

is approved in partial fulfillment of the requirements for the degree of

Master of Science – Geoscience
Department of Geoscience

Henry Sun, Ph.D.
Examination Committee Chair

Ganqing Jiang, Ph.D.
Examination Committee Member

Oliver Tschauner, Ph.D.
Examination Committee Member

Michael Pravica Ph.D.
Examination Committee Member

Jaeyun Moon, Ph.D.
Graduate College Faculty Representative

Alyssa Crittenden, Ph.D.
*Vice Provost for Graduate Education &
Dean of the Graduate College*

Abstract

This study arose from an accidental discovery of calcite spherulites forming on colonies of various halophilic bacteria grown on solid Luria-Bertani medium made containing water from a brine pool in Death Valley, their natural habitat. Further studies with a large spherulite forming bacteria, *Pseudoalteromonas haloplanktis*, showed that calcite precipitation conditions were the consequence of bacteria using amino acids as a source of carbon and energy, a metabolism that produces NH_3 and CO_2 waste products. NH_3 raises the pH of the medium, turning CO_2 into CO_3^{2-} . Calcium in the natural brine combines with CO_3^{2-} . The resulting spherulitic calcite precipitation is nano-acicular due to organo-mineral interactions with amino acids. As the bacterial colony grows larger in size, new rows of calcite spherulites emerge outside the old row and a few millimeters inside the colony's active edge. Starvation kills bacteria in the colony center. Living bacteria degrade dead bacteria recycling them for energy, a process that expels PO_4^{3-} as well as NH_3 and CO_2 into the medium. PO_4^{3-} eventually reaches inhibitory levels that stop further calcite spherulite growth. Calcite spherulite growth eventually resumes once inhibitory PO_4^{3-} was removed by struvite precipitation. Calcite growth resumed then switched to micro-prismatic until the precipitation of orange guanine monohydrate at the colony center, at this time, 3-fold calcite coats spherulites. This study sheds light on the formation and inhibition of calcite spherulites found with infection induced urolithiasis, a medical condition referring to stone obstructions in the human urinary tract. Similar formations are also found in mollusks and stromatolites. All these examples are morphologically similar due to the inevitable presence of amino acids, peptides, or proteins with various degrees of biological control. A case is made that understanding simpler bacterial biomineralization processes can also illuminate formation processes of the more complex.

Acknowledgements

I would like to thank my advisor, Dr. Henry Sun, for helping guide me during a hectic pandemic. Dr. Sun provided his extensive knowledge in microbiology, and hundreds of hours of his time to help make this wonderful project possible.

Dr. Oliver Tschauner for his extensive teachings in my favorite subject mineralogy and for helping me get our samples analyzed during the pandemic. Furthermore, the rest of my committee Ganqing Jiang, Michael Pravica, and Jaeyun Moon for their guidance and knowledge.

Dr. Minghua Ren, Dr. Hexiong Yang, Dr. Robert Downs, and Dr. Monica Arienzo, for opening their laboratories to me during those difficult times and the hours of their time given with extensive patience for my scientific tasks.

NASA EPSCoR for funding my research through the Life in Salts project: a multidisciplinary investigation of microorganisms and biosignatures in the Death Valley Salt Pan.

Last but not least, a thanks to my wife and parents for always supporting my obsession for science.

Table of Contents

Abstract.....	iii
Acknowledgements.....	iv
Table of Contents.....	v
List of Figures.....	viii
Chapter 1: Figures.....	1
Chapter 2: Introduction.....	14
2.1 Abiotic CaCO ₃ Spherulites.....	14
2.2 Biotic CaCO ₃ Spherulites.....	15
2.3 Liquid Culture CaCO ₃ Spherulites.....	16
2.4 Experimental Summary.....	17
2.5 Relevance to Nature.....	17
Chapter 3: Materials and Methods.....	19
3.1 Bacterium Isolation and Sequencing.....	19
3.1.1 Bacterium Isolation.....	19
3.1.2 16S rRNA Amplification and Sequencing.....	19
3.1.3 Phylogenetic Analysis.....	20
3.2 Liquid Media Sampling and Analysis.....	20
3.3 DAPI Staining.....	21
3.4 SEM Imaging Bacteria.....	21
3.5 ToF-SIMS.....	22
3.6 ATR-FTIR.....	22

3.7 Brine Composition	22
3.8 SEM-EDS of Precipitates	23
3.9 X-ray Crystallography	23
3.9.1 Single Crystal X-ray Diffraction	23
3.9.2 Synchrotron Microdiffraction.....	23
Chapter 4: Experimental Results	25
4.1 Mineral Formation on Bacterial Colonies.....	25
4.2 Mineralogy of Precipitates	26
4.2.1 Calcite Spherulites.....	26
4.2.2 Struvite	28
4.2.3 Guanine Monohydrate.....	28
4.3 Identification of Bacteria	29
4.4 pH Increase	29
4.5 pH Tolerance.....	29
Chapter 5: Discussion	30
5.1 Overlap with Nature.....	30
5.2 Effect of Carbohydrates	30
5.3 Spherulite Formation on Colonies	31
5.4 PO ₄ ³⁻ Induced Stoppage	32
5.5 Three-fold Layer on Spherulites	33
Chapter 6: Relevance to Nature Discussion.....	36
6.1 Spherulites in Mollusks.....	36
6.2 Spherulites in Stromatolites	37

6.3 Struvite and Calcite in the Urinary Tract	38
References	40
Curriculum Vitae	45

List of Figures

Figure 1 Calcite Crystallography:	1
Figure 2 Spherulite Evolution:	2
Figure 3 PH and Bacterial Growth Versus Time:	3
Figure 4 Calcite Spherulite Formations:	4
Figure 5 Guanine Monohydrate:	5
Figure 6 Bacteria New Versus Old:	6
Figure 7 X-ray Diffraction of Calcite:	7
Figure 8 Tof-SIMS of Guanine Monohydrate:	8
Figure 9 ATR-FTIR of Guanine Monohydrate:	9
Figure 10 Phylogenetic Tree:	10
Figure 11 PH Tolerance Graph:	11
Figure 12 PH Gradient:	12
Figure 13 DAPI Stain:	13

Chapter 1: Figures

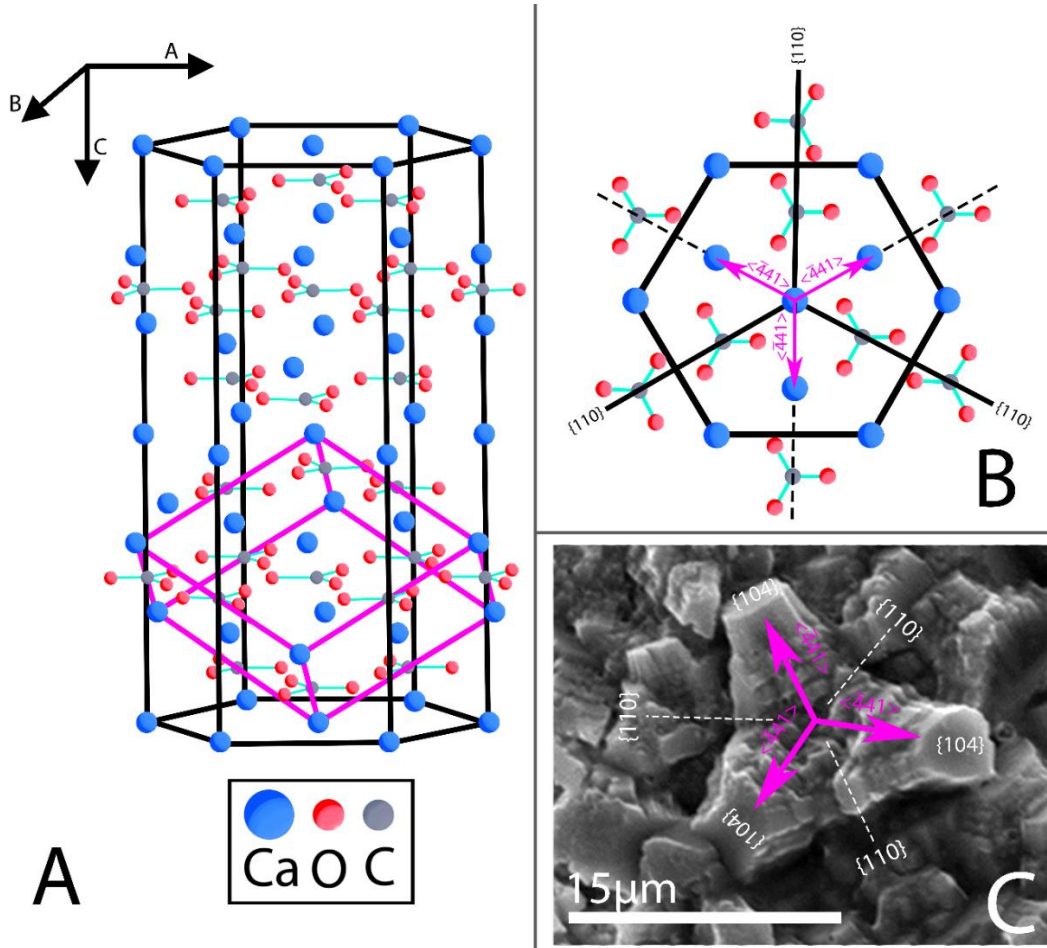


Figure 1 | Calcite Crystallography: A.) Computer rendering of calcite rhombohedral unit cell with hexagonal unit cell overlay. Oxygens of CO_3^{2-} are exposed perpendicular to the c -axis B.) Looking at a slice of down the c -axis, one can see the three strongest growth directions $\langle \bar{4}41 \rangle$ and the three most inhibited directions {110}. C.) 3-fold unit coating outermost spherulites with the proposed crystallographic growth directions labeled.

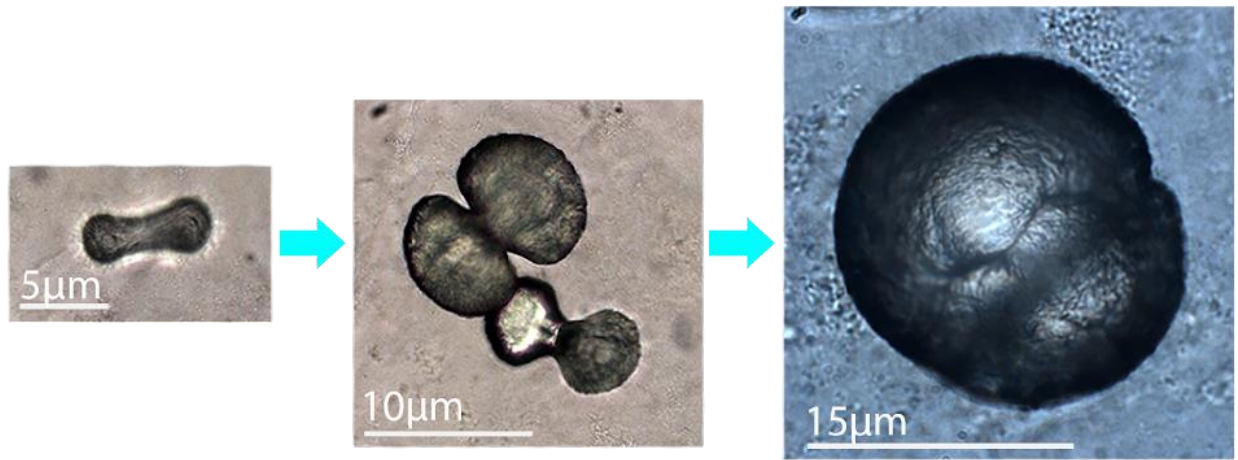


Figure 2 | Spherulite Evolution: Light micrographs, evolution of calcite spherulites from a bundled precursor. Synonymous with a category 2 spherulite growth sequence.

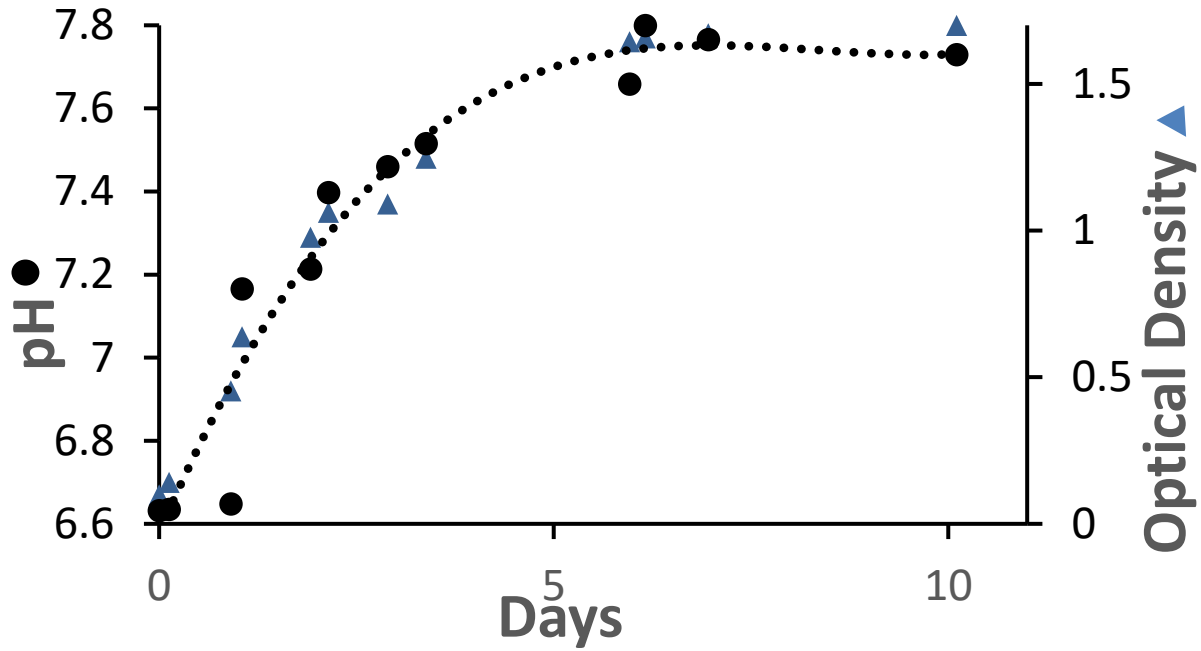


Figure 3 | PH and Bacterial Growth Versus Time: Bacterial growth blue triangles (Optical Density at 600nm) and pH black dots vs time graph. Showing relation of bacterial growth to pH change. Despite exponential bacterial growth, pH didn't rise substantially until after day 1, due to the consumption of carbohydrates.

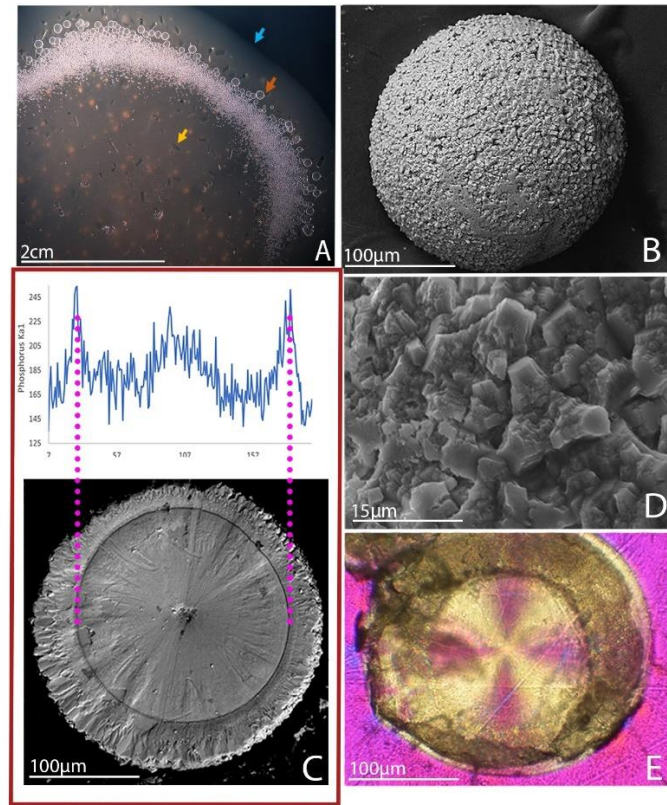


Figure 4 | Calcite Spherulite Formations: A) light micrograph of 4-month-old colony showing the edge of colony (blue arrow), spherulites (orange arrow) formed, accompanying struvite crystal formations (yellow arrow), and guanine monohydrate (orange opaque balls) B) SEM micrograph showing a close-up of spherulite surface (sampled from the same colony) C) SEM micrograph of bisected spherulite showing nanocrystalline core and micrometric outer layer, demarcated by a dark circular abrupt transition; EDS line scan showing concentration of phosphorus: Rapid decrease with spherulite growth is followed by stasis, an abrupt rise at the transition, and a decline again with the growth of the prismatic layer. (Sampled from the same colony) D) Zoomed in SEM micrograph of 3-fold unit that coats the spherulite above (pictured in B) E) Cross polarized image of polished bisected spherulite, Maltese cross indicates all crystallites are oriented with radial crystallographic symmetry to the nucleus.

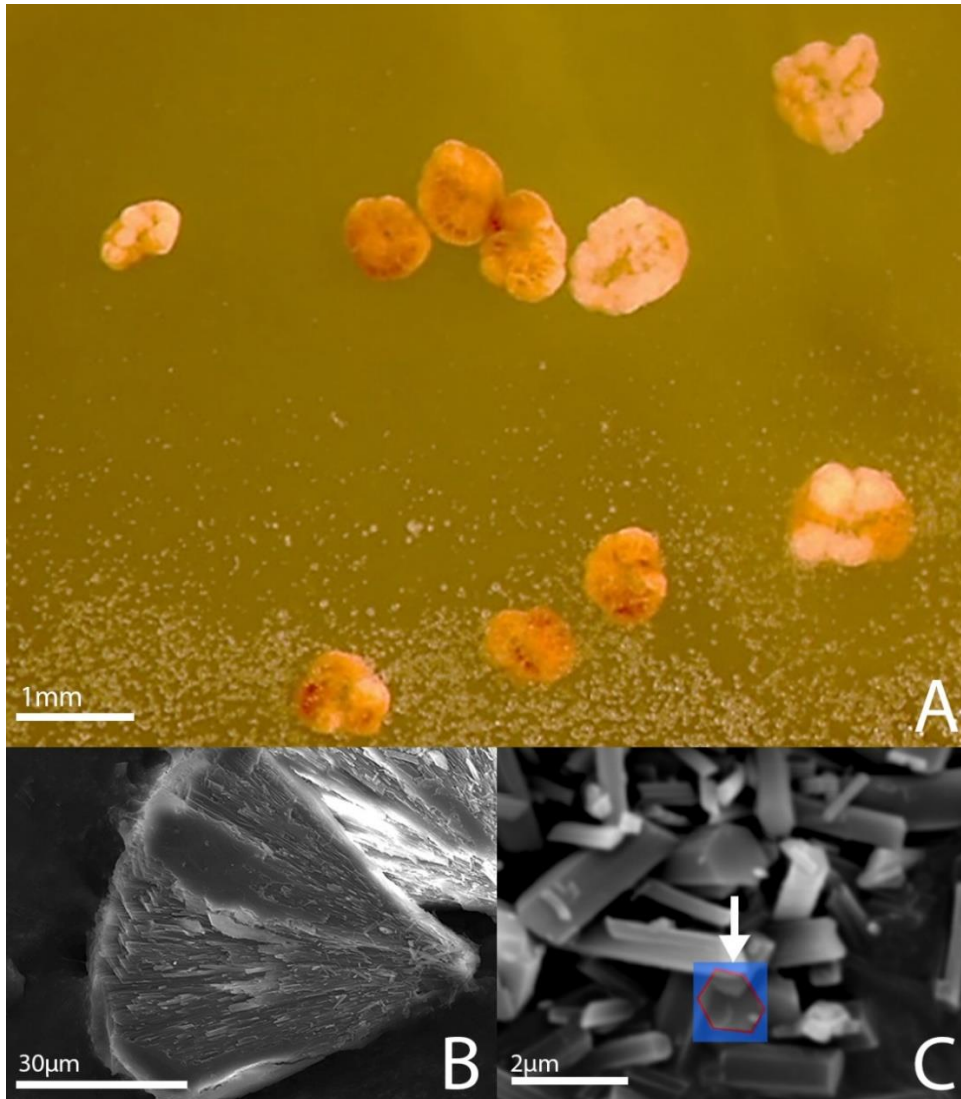


Figure 5 | Guanine Monohydrate: A) Light micrograph of guanine monohydrate globular spherulites on colony center, solid media, 4-months after inoculation. B) SEM micrograph of a cleaved guanine monohydrate revealing a crystalline spherulitic interior. C) SEM micrograph of guanine monohydrate revealing symmetry usually found in biogenic anhydrous guanine.

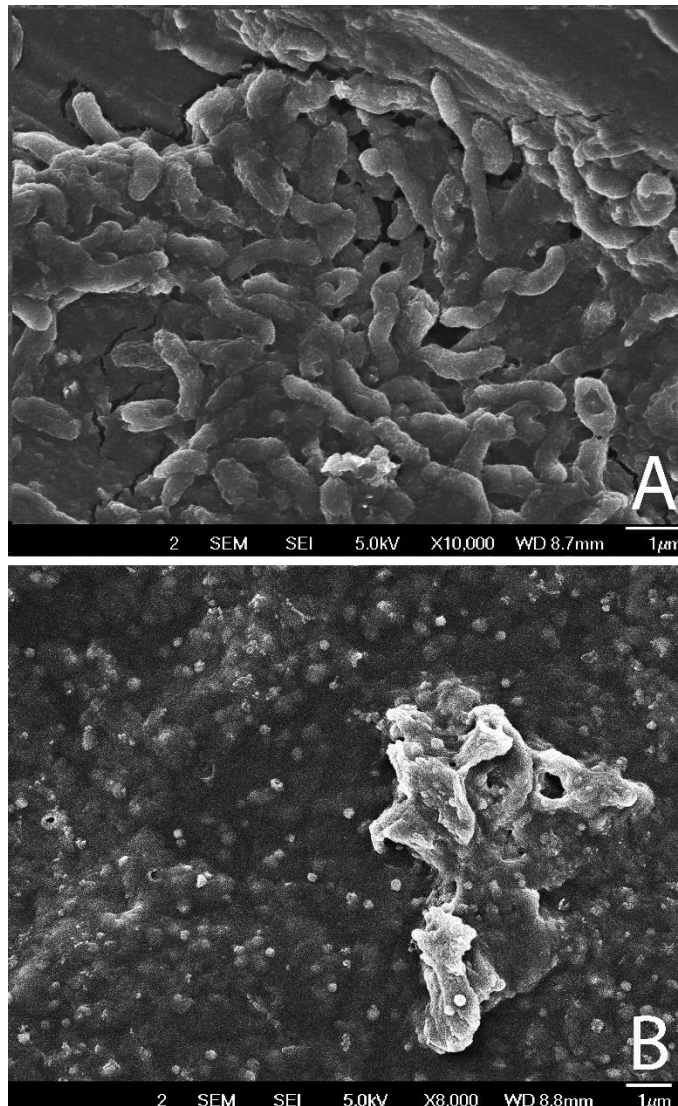


Figure 6 | Bacteria New Versus Old: Field SEM image of *Pseudoaltermonas haloplanktis* bacteria. A) 7-day old healthy bacteria collected during active calcite spherulite precipitation. B.) 3-month-old cell wall fragments in white, surrounded by $\sim 0.25\mu\text{m}$ nodules of guanine monohydrate.

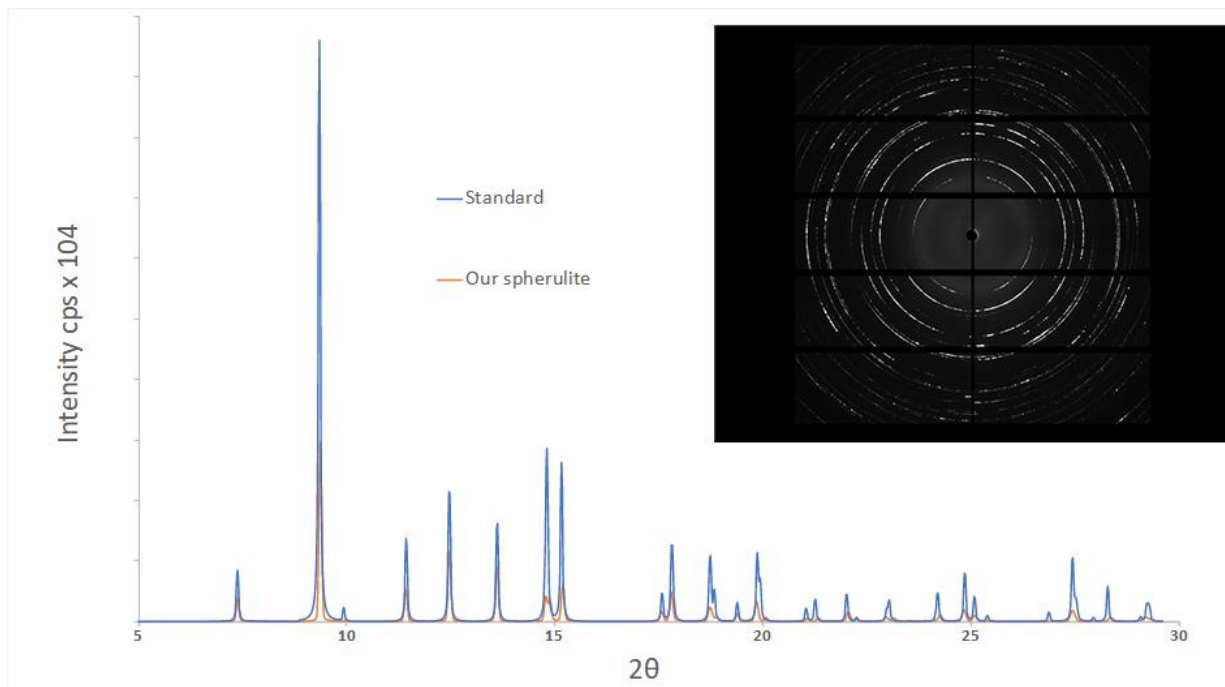


Figure 7 | X-ray Diffraction of Calcite: XRD stack showing match of bacterially generated calcite spherulite (orange) and low Mg^{2+} calcite standard (blue).

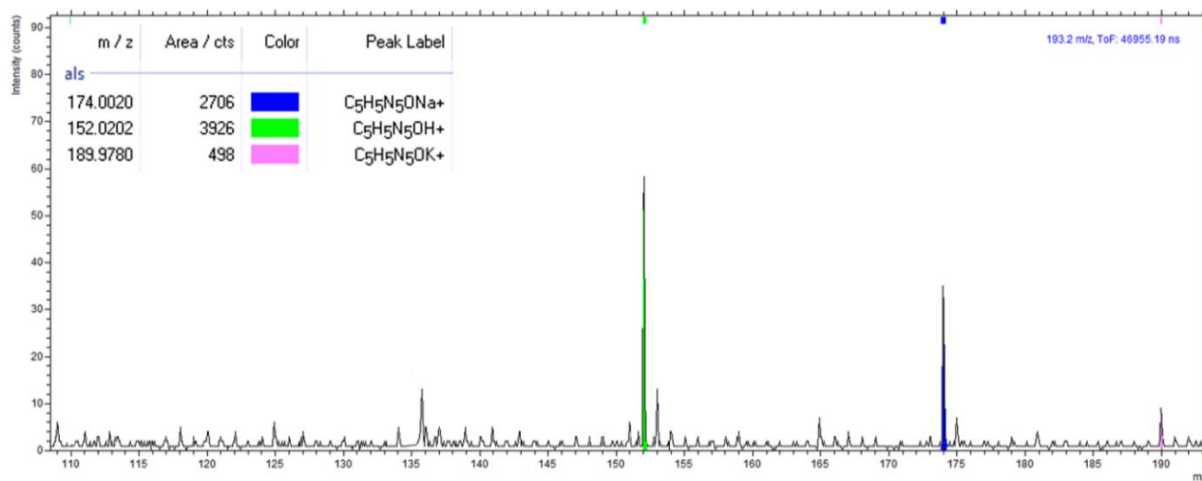
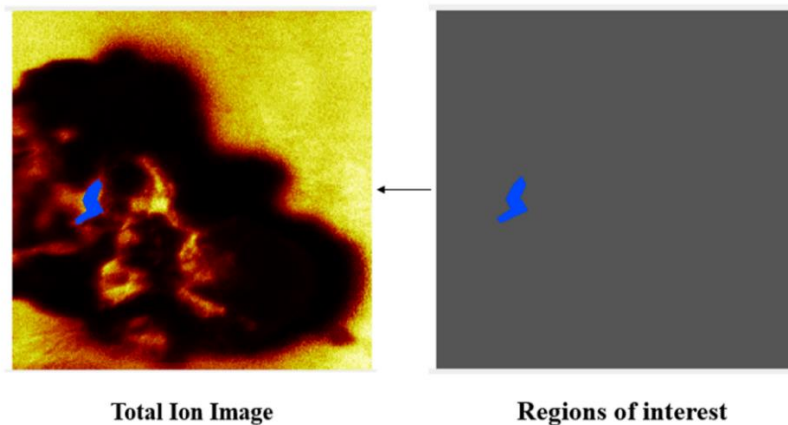


Figure 8 | ToF-SIMS of Guanine Monohydrate: ToF-SIMS matched guanine ($C_5H_5N_5O$) with K^+ , Na^+ , and H^+ . Analyzed region (in blue) is where a fresh crystalline pocket was exposed. K^+ and Na^+ were contaminations.

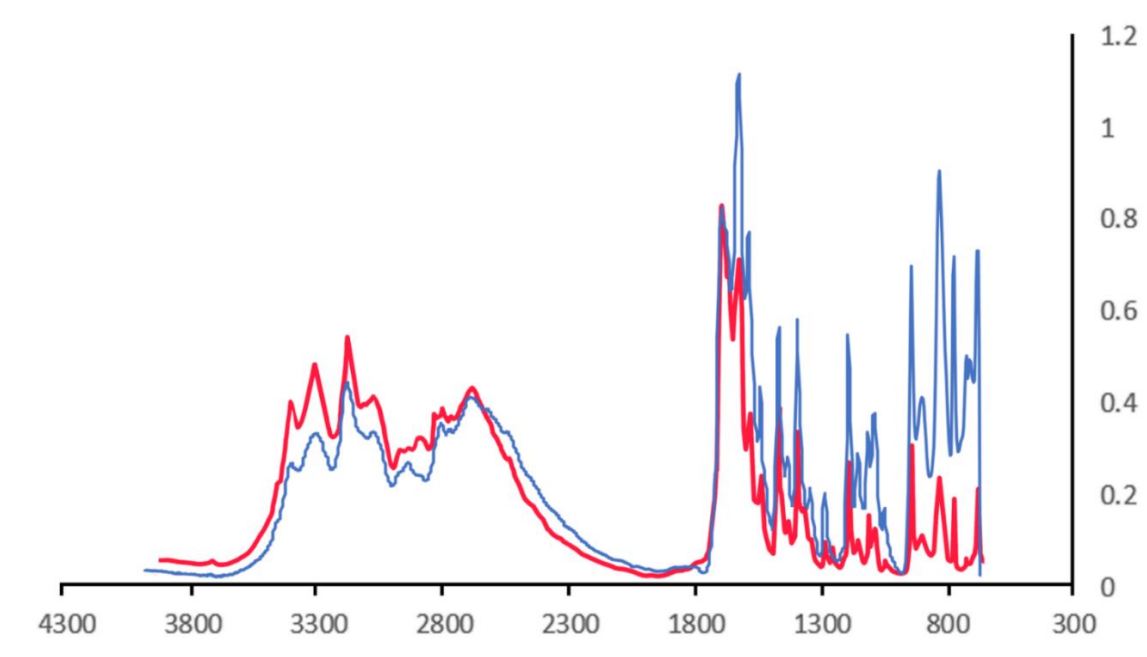


Figure 9 | ATR-FTIR of Guanine Monohydrate: ATR-FTIR absorption spectra overlay of pure standard guanine monohydrate (red) and guanine monohydrate spherulites from *Pseudoaltermonas haloplanktis* colonies (blue).

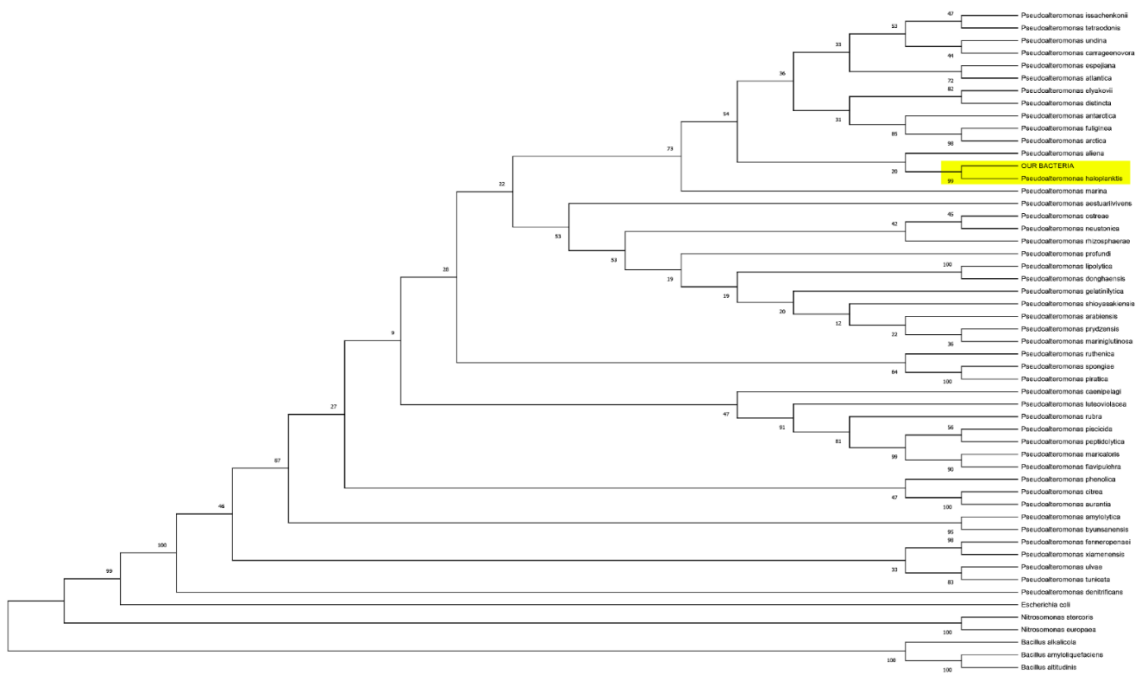


Figure 10 | Phylogenetic Tree: Phylogenetic tree highlighting “OUR BACTERIA” as *Pseudoaltermonas haloplanktis* with 99% similarity. *Pseudoaltermonas haloplanktis* is a marine bacterium also found in halophilic environments like Badwater, Death Valley. All other species of *Pseudoaltermonas* are listed as neighbors along with *E. coli* and *Bacillus* for reference.

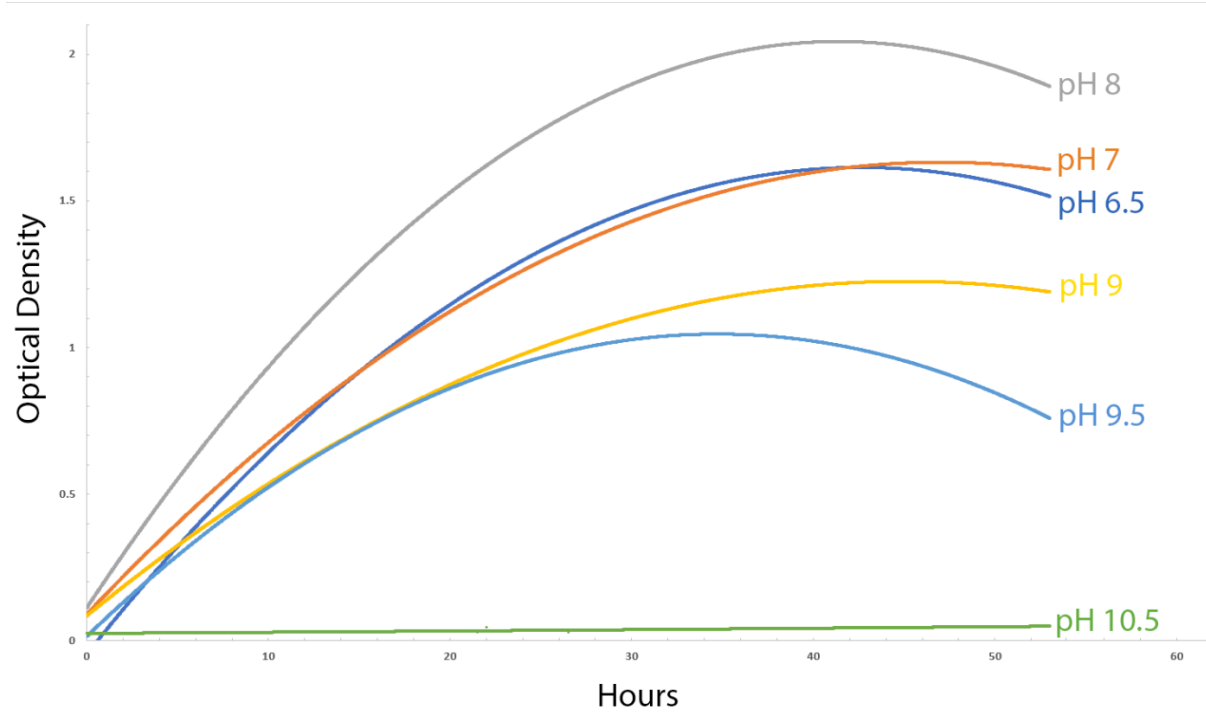


Figure 11 | PH Tolerance Graph: pH tolerance of *Pseudoaltermonas haloplanktis* in buffered media with population estimated via the turbidimetric method.

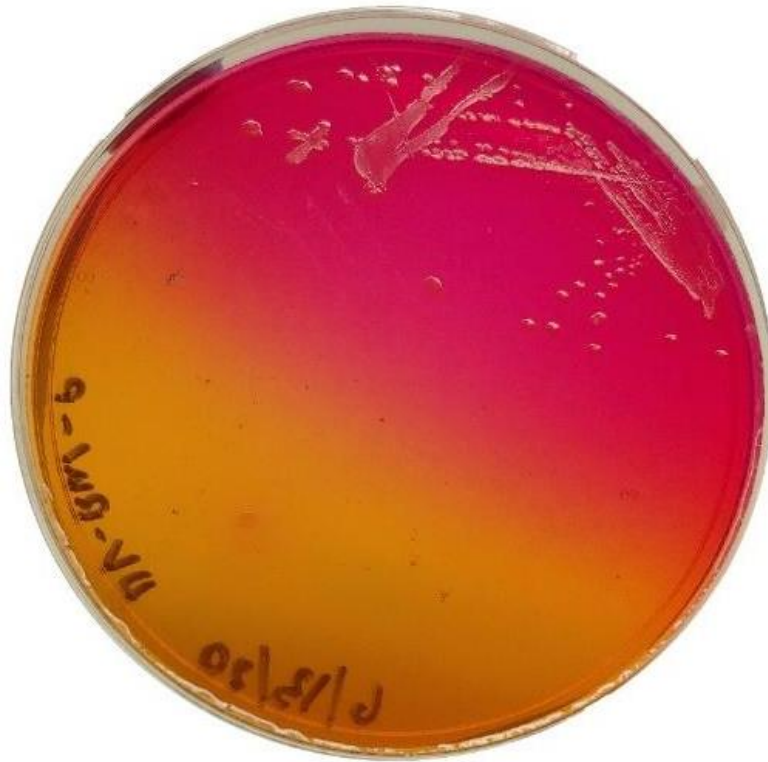


Figure 12 | PH Gradient: Increase in pH is due to bacterial activity, as indicated by the change of color of added pH indicator phenol red from yellow (pH < 8) to red (pH > 8). A pH gradient is clear 4 days after inoculation.

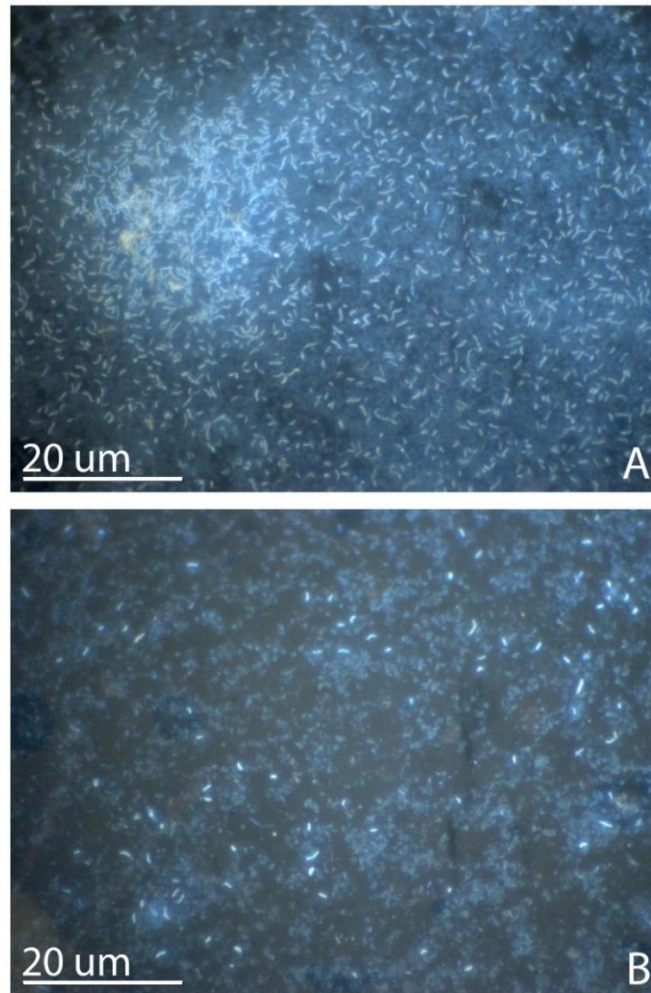


Figure 13 | DAPI Stain: Photomicrograph of DAPI stained bacteria, bacteria will glow bright if their cell walls are intact. A.) Day 10, during calcite spherulite core formation, the colony still mainly consisted of intact cells. B.) Day 30, when struvite precipitates, most cells are dead and lysed.

Chapter 2: Introduction

2.1 Abiotic calcite spherulites

CaCO₃ spherulites are a result of extreme anisotropic crystal growth, where CaCO₃ precipitates as nanofibers. Under rapid abiotic conditions, calcite spherulites do not form. Rather, spherulitic vaterite, a metastable nano sized polymorph of CaCO₃ forms instead (Liu and Yates, 2006)(Konopacka-Łyskawa et al., 2019). Crystal growth of vaterite is inherently anisotropic, due to growth along its *c*-axis being fastest, i.e., requiring the least amount of energy to grow (Pokroy et al., 2015). This is due to stacking faults in the *c*-axis of vaterite lowering the energy for further growth in that direction (Qiao and Feng, 2007). The newest model of vaterite's controversial structure agrees with this explanation, showing that the "most likely" vaterite unit cell has abundant stacking faults in the *c* direction $\langle 001 \rangle$ (Christy, 2017). Lowered energy in the *c* growth direction results in highly unidirectional growth and thus the formation of nanocrystalline fibers. The surfaces of nanomaterials are highly energetic, causing them to grow in bundles initially and spheres ultimately via growth front nucleation (GFN). GFN refers to crystal structures that form due to crystals nucleating on the exposed ends of existing crystals with a differing crystal orientation to its parent crystal (Dominguez Bella and Garcia-Ruiz, 1986; Granasy et al., 2007; Zhou et al., 2011). Initial GFN causes branching between 0-30 degrees, causing further growth to progressively splay out and fill gaps (Pokroy et al., 2015). Once a sphere is formed, the angle of branching becomes smaller (0-5°) only branching when space is provided (Marangoni and Ollivon, 2007). The above describes a category 2 spherulite formation sequence (Granasy et al., 2007).

Vaterite spherulite can transform to calcite spherulites in several days after forming (Liu and Yates, 2006).

2.2 Biotic CaCO₃ Spherulites

In the presence of amino acids, calcite spherulites can form directly, i.e., without first forming as a vaterite spherulite (Braissant et al., 2003). Unlike the formation of vaterite spherulites, where unidirectional growth is controlled by extreme precipitation conditions, the direct formation of calcite spherulites is due to adsorption of amino acids preventing further crystal growth. The adsorption is electro-static, between the positive potential of the amino acids' amine groups (-NH₂) and the negative potential of the three oxygens in the carbonate ions (CO₃²⁻) of calcite (Kai et al., 2002). Not all calcite planes exhibit equally exposed oxygen from CO₃²⁻. The CO₃²⁻ ions have a trigonal planar configuration, with the three corners being oxygens and the carbon atom at the center. A calcite crystal consists of these planar carbonate ions with stacking order in the *c*-direction (Figure 1A). Thus, faces that are perpendicular to the *c*-axis are relatively rich in exposed oxygen with the highest electrostatic potential for inhibition (Figure 1A). Consequently, amino acids adsorb and inhibit only planes that are perpendicular to *c* (Mann et al., 1990; Albeck et al., 1993). This inhibition results in highly elongated calcite nanocrystals, shaped similarly to the previously mentioned vaterite. While calcite spherulites aren't elongated due to stacking faults, the same GFN growth mechanism follows, resulting in a category 2 spherulite sequence (Figure 2). Thus, in the presence of amino acids, or molecules containing an amine group, calcite spherulites form, even under slower precipitation conditions otherwise conducive to the more

familiar {104} rhombohedral growth habit.

2.3 Liquid Culture CaCO₃ Spherulites

Both vaterite and calcite spherulites have been shown to form biologically in liquid bacterial cultures as a result of bacteria using amino acids as a source of carbon (Rodriguez-Navarro et al., 2007). If sugars or carbohydrates are available, bacteria use amino acids as a nitrogen source and assimilate them into their cell components instead. In the absence of sugars and carbohydrates and if amino acids are available in abundance, most of the amino acids are metabolized as a carbon source. That metabolism begins with a step called deamination, where the amine group (-NH₂) is removed and discarded as waste. The remaining carbon skeleton, an α -keto acid, enter the Krebs cycle where it is oxidized to CO₂ to yield energy. Therefore, unlike bacterial oxidation of carbohydrates, which produces CO₂ waste, bacterial oxidation of amino acid produces NH₃ as well as CO₂ as waste. The NH₃ raises the pH of the medium to values as high as 7.8 (Figure 3), turning it into an alkaline trap for CO₂ (Rodriguez-Navarro et al., 2007). If the medium contains sufficient amounts of calcium, it will ultimately become saturated with respect to CaCO₃. Biological transport systems have a limit, so there are always amino acids present in the medium when CaCO₃ precipitation occurs. In a vigorously stirred, well mixed liquid culture all dissolved species and bacteria, which can nucleate carbonate minerals, are homogenously distributed. Because of this, all cells will start to grow and stop growing at the same time. As a result, a large number of small spherulites (0.5–5 μ m) of equal size form (Rodriguez-Navarro et al., 2007). Also, a well-mixed liquid medium supports rapid logarithmic bacteria growth and thus rapid production of NH₃ and

CO₂. Hence, spherulites formed in liquid bacteria cultures are often originally vaterite.

2.4 Experimental Summary

In this study, I show that calcite spherulites form on top of the colonies of a halophilic bacteria grown on solid Luria-Bertani medium, with formation dynamics different from those in liquid culture, more similar to systems in nature. Unlike in liquid cultures, where the formation of spherulites is synchronous, the formation of spherulites on agar cultures occurs in rows of increasing size, in agreement with colony growth dynamics (Figure 4A). On solid media, the surrounding agar becomes depleted in nutrients over time, this ultimately brings colony growth to a stop. In addition, I also made an interesting observation toward the end of colony growth where the growth of spherulites is interrupted by phosphate. Specifically, as the colony approached its size limit, the cells in the center of the colony were already dead, lysed, and degraded. This process produces PO₄³⁻ in addition to CO₂ and NH₃ as waste. Subsequent struvite (MgNH₄PO₄•6H₂O) formation removed PO₄³⁻ from the colony's environment and calcite spherulite growth resumed. Lastly a final 3-fold calcite coating formed as a result of low supersaturation just before the complete end of bacterial life within the colony. This formation coincided with recalcitrant orange guanine monohydrate precipitation in the colony center.

2.5 Relevance to Nature

Why is it important to study CaCO₃ spherulites? CaCO₃ spherulites are synthesized by mollusks

as a rapid growth tool for shell repair, invader entombment, and quick shell growth. They are also building blocks of stromatolites, the oldest microbial trace fossil, found in sedimentary records throughout the history of the planet from the Eoarchean Era, 3.5 billion years ago, to today. On modern earth, stromatolites are associated with cyanobacteria-dominated microbial mats, the exact role of biology remains poorly defined. CaCO_3 spherulites are also present in the urine of patients who suffer from urinary tract infections (UTI's) and struvite stone obstructions (urolithiasis). The presence of CaCO_3 spherulites in urine could possibly be used as an inexpensive diagnostic. In the discussion section, I will comment on these three cases of biogenic CaCO_3 spherulites based on discoveries from this study.

Chapter 3: Materials and Methods

3.1 Bacterium Isolation and Sequencing

3.1.1 Bacterium Isolation

Bacterium was isolated from brine water samples collected in sterile containers from Badwater Basin, Death Valley, California. Isolation was done using the quadrant streak plate method on solid media containing 15.0g agar, 10.0g Luria-Bertani, and 1L of collected Death Valley brine autoclaved and filtered to 0.2 μ m. Isolated bacterium was rod-shaped (0.2 to 1.5 by 1.8 to 3 μ m) aerobic, motile, halophilic, and gram-negative.

3.1.2 16S rRNA Amplification and Sequencing

The full 16S rRNA gene was amplified with polymerase chain reaction (PCR) using a universal bacterium forward 9bF (GRGTTTGATCCTGGCTCAG) and reverse 1512uR (ACGGHTACCTTGTTACGACTT) primers (Eder et al., 1999). Cells were sampled from a single colony in duplicate to reduce PCR bias and suspended in 20 μ L Lyse-N-Go reagent. Samples were then incubated at 98 $^{\circ}$ C for 10 min to cleave cells and expose DNA. Resulting lysed cells were diluted in 80 μ L of deionized nuclease free water. Resulting slurry was centrifuged at 6000 rcf for 10 min to remove cell fragments. With 10 μ M of primer, the PCR mixture were placed in a Techne TC-5000 thermal cycler for an initial denaturation at 96 $^{\circ}$ C for 90 s, followed by: ten cycles of 96 $^{\circ}$ C for 30 s, 60 $^{\circ}$ C for 30 s, and 72 $^{\circ}$ C for 1 min; 25 cycles of 94 $^{\circ}$ C for 20 s, 60 $^{\circ}$ C for 30 s, and 72 $^{\circ}$ C for 1 min (+2 s for each further cycle); and a final incubation at 72 $^{\circ}$ C for 10 min. PCR products (5 ml) were analyzed by agarose gel electrophoresis (1.0%). Gene sequences were

determined on an ABI 3130 genetic analyzer at the Nevada Genomics Center, Las Vegas.

3.1.3 Phylogenetic Analysis

The resulting nearly full-length sequence of the 16S rRNA gene was grouped at 99% similarity on NCBI and analyzed using the BLAST algorithm (McGinnis and Madden, 2004) to identify the most similar species. A phylogenetic tree was constructed by means of the neighbor joining method (Saitou and Nei, 1987). The percentage of replicate trees in which the associated taxa clustered together in the bootstrap test (1000 replicates) are shown next to the branches (Felsenstein, 1985). The evolutionary distances were computed using the p-distance method (Kumar et al., 2000). This analysis involved 53 nucleotide sequences. All positions with less than 98% site coverage were eliminated, i.e., only those with fewer than 2% alignment gaps, missing data, and ambiguous bases were allowed at any position (partial deletion option). There were a total of 1046 positions in the final dataset. Analyses were conducted using MEGA-X (Tamura et al., 2007, 2021).

3.2 Liquid Media Sampling and Analysis

To monitor population and the evolution of pH over time, liquid media was prepared with 10g Luria-Bertani and 1 L of distilled water autoclaved and filtered to 0.2 μm . Under a sterile laminar flow hood, media was placed into two sterile 1000 ml Erlenmeyer flasks and sealed with parafilm. One was inoculated with *Pseudoalteromonas haloplanktis* and the other left uninoculated (control). Daily, under laminar flow hood, Erlenmeyer flasks were opened, and a 10 ml liquid sample was withdrawn with a sterile pipet for pH and turbidity analysis. pH was analyzed with a pH electrode, accumet AB15 pH meter that has a pH range of -2 to 20 with an error of ± 0.05 . The

turbidimetric spectrometer method (Nath and Koch, 1970) was used to approximate population growth. The same 10 ml liquid sample was placed into a quartz cuvette and absorbance was measured using a Hach DR6000 at a wavelength of 600 nm. Nano pure distilled water was used to zero the machine before each measurement. Bacterial pH tolerance was determined in the same way described above but first buffering each batch with Good's buffers. pH and respective buffer: 6.5 (Pipes), 7 (Hepes), 8 (Tris), 9 (Ampso), 9.5 (Ches), and 10.5 (Caps). Each inoculated with *Pseudoalteromonas haloplanktis*. There was no measurable pH shift from start to finish of the experiment.

3.3 DAPI Staining

In parallel a sterile stainless-steel needle was dipped vertically into isolated colonies of 10-day and 30-day old plates. Each were placed onto glass slides and allowed to air dry. Bacterial samples were stained with DAPI ($0.01 \mu\text{g ml}^{-1}$) to distinguish intact bacteria from cellular debris (Porter et al., 2007). The samples were rinsed in demineralized water, air dried, and viewed with an epifluorescence microscope equipped with UV, DAPI, fluorescein excitation filter set for DAPI counts.

3.4 SEM Imaging Bacteria

Bacteria were picked from single colonies of a 1-week-old plate and a 3-month-old plate, with sterile swabs. Two sterile aluminum slides were separately swabbed with one or the other and allowed to dry. Slides were placed into a JEOL JSM-6700F Field Emission Scanning Electron Microscope (FE-SEM) in the Electron Microanalysis and Imaging Laboratory (EMIL) at UNLV.

3.5 ToF-SIMS

For compositional identification of orange globular guanine monohydrate (Figure 4a and Figure 5a), time of flight secondary ion mass spectroscopy (ToF-SIMS) was done by a technician at the Montana State University Imaging and Chemical Analysis Laboratory using a Cameca ION TOF IV with a mass resolution of 0.001 and a mass range of 0-10,000 amu. ToF-SIM spectra were obtained for an exposed crystal face on the sample dropped onto a Si wafer as a control. Work was done at the Imaging and Chemical Analysis Laboratory at the Montana State University.

3.6 ATR-FTIR

To confirm hydration state and mineralogy of guanine results from ToF-SIMS, an FTIR absorption spectra was collected off an exposed crystal face (on glass slide) with a MicroFTIR (Nicolet iN10 MX, Thermo Fisher, USA), on ATR and cooled mode. The spectrum was set to the range of 4000 – 650 cm^{-1} and scanned 128 times at a resolution of 8 cm^{-1} with a collection time of 25s per frame. Atmospheric CO_2 and glass slide background were collected and removed before the primary analysis and rescanned every 100 minutes. For background removal and baseline correct OMNIC software was used. Work was done at microplastics lab, Desert Research Institute Reno.

3.7 Brine Composition

Death Valley natural brine was sent to UNR's Core Analytical Laboratory for water analysis. Ionic concentrations were determined with a Dionex ICS-3000 ion chromatograph. Constituents with error < 5% (mg/l): Ca: 981, Mg: 240, K: 720, Na: 6294, SO_4 : 2921, and Cl_2 : 6418.

3.8 SEM-EDS of Precipitates

Precipitates were placed on sticky carbon-coated stubs attached to aluminum sample holders. Samples were gold coated. The elemental compositions of precipitates were determined by means of energy-dispersive X-ray spectroscopy, (EDS). Using a JEOL 5600 Scanning Electron Microscope. All precipitates were sputter gold coated before analysis.

3.9 X-ray Crystallography

3.9.1 Single Crystal X-ray Diffraction

For crystal structure determination, of struvite, a single crystal was selected, mounted on a glass fiber and aligned on a Bruker D8 Apex diffractometer equipped with a 4K APEX 2 CCD detector with graphite monochromatized Mo(K) radiation ($\lambda = 0.71069 \text{ \AA}$). Individual frames were measured with widths of $0.5^\circ\omega$ and an acquisition time of 30s per frame. The intensity data were corrected for X-ray absorption using the Bruker program SADABS. No. of reflections collected 11431, No. of independent reflections 2352. Unit cell: $a = 6.961$, $b = 6.150$, $c = 11.249 \text{ \AA}$. Space group $Pmn2_1$. R_1 : 0.055, wR_2 : 0.092, R_{int} : 0.028 Goodness-of-fit 1.087. 2θ range for data collection ≤ 65.00 .

3.9.2 Synchrotron Microdiffraction

Calcite spherulite diffraction data was collected by a technician at the microdiffraction beamline 12.3.2 (Berkeley Lab's Advanced Light Source), using a monochromatic X-ray beam with $\lambda = 0.4959 \text{ \AA}$ (25 keV) in angle-dispersive transmission mode. Detector distance and orientation were

calibrated using a cubic crystalline CeO₂ standard. Calibration, integration and correction for geometric distortion was conducted with DIOPTAS (Prescher and Prakapenka, 2015). Structure was determined using GSAS-II software (Toby and von Dreele, 2013).

Chapter 4: Experimental Results

4.1 Mineral Formation on Bacterial Colonies

I followed the formation process of calcite spherulites on LB agar under the light microscope after inoculation of the bacterium and incubation at 25 °C. Small dumbbell spherulitic precursors, about 10 μm in diameter, appeared on the colony just inside its edge by day two (Figure 4A). Their nucleation and growth followed this sequence: bundles of needles, sheaf of wheat, dumbbells, spheres. This sequence is known as the category 2 spherulite evolution (Granasy et al., 2007; Pusztai et al., 2008). The “dumbbells” always transitioned to round spherulites before reaching a size of 20 μm. By day three, spherulites forming on the very edge became large enough to be visible to the naked eye, forming a ring with a spherulite free colony center (Figure 4A). Spherulite growth and enlargement stopped when a new row of spherulites formed. This succession of growth of existing spherulites and inhibitive formation of new spherulites continued as the colony grew larger, resulting in a band of spherulites. A large number of small calcite spherulites formed when the colony was smaller (innermost spherulites figure 4A) compared to a smaller number of large spherulites when the colony became larger (orange arrow figure 4A). There was a zone just inside the colony edge that was not conducive to carbonate precipitation (Figure 4A between orange and blue arrows). This zone became wider as the colony grew larger. In other words, as the colony grew bigger, the conditions that triggered new spherulite nucleation occurred farther and farther away from fresh agar. After day 20, spherulite nucleation and growth seized. Around one month, struvite crystals visible to the naked eye appeared in the center of the colony (Figure 4A yellow arrow). The spherulites in the outermost ring resumed growth, adding a 20 μm thick layer of

nanocrystals to the dark circular demarcation in Figure 4C. Further precipitation added a 30-50 μm layer of prismatic 3-15 μm thick calcite crystals, preferentially to the side of the spherulites that faced the colony edge, not on the side that faced the colony center. As shown by SEM-EDS analyses of bisected spherulites taken from the colony edge, the pause and resumption of carbonate precipitation in the outermost row of spherulites produced in them a circular electron-dense layer that is enriched in phosphate (Figure 4C). Around month three, prismatic calcite growth stopped, seen by periodically bisecting spherulites (figure 4C). A new regime of carbonate precipitation began, coating the spherulites in the outermost row with 3-fold calcite monocrystals (Figure 4D). At this time, globular spherulites of guanine monohydrate appeared at the center of the colony (Figure 6B). Later, they appeared throughout the colony (Figure 4A and figure 5A). Around month six, calcite spherulites began to dissolve back into agar, becoming disc shaped. Guanine monohydrate was not affected. Guanine monohydrate continued to grow, until about 1mm in diameter (Figure 5), at which point the experiment was terminated.

4.2 Mineralogy of Precipitates

4.2.1 Calcite Spherulites

SEM-EDS analyses revealed peaks of Ca ($K\alpha$ 3.69), O ($K\alpha$ 0.525), and C ($K\alpha$ 0.277), likely indicating a phase of CaCO_3 . Synchrotron X-ray microdiffraction yielded a refined unit cell of $a = 4.9940$ (9), $b = 4.9940$ (9) ($b = a$ because trigonal), and $c = 17.1075$ (1), $\text{Alpha} = 90$, $\text{Beta} = 90$, $\text{Gamma} = 120$, machine error $< - 0.002$, $\text{rmse} = 0.00001629669$. consistent with cell parameters of calcite. Previous studies have shown that vaterite spherulites could transform into calcite spherulites. This is not the case in cultures in this study. The spherulites described here are

originally calcite based on three lines of evidence. First, synchrotron X-ray microdiffraction detected no other phases, nor evidence of vaterite from refinement (Figure 7). Second, the precipitation rate in our culture is likely far too slow for vaterite formation. Third, if the spherulites described here were originally vateritic and transformed to calcite, there would be a detectable volume change. Vaterite has a smaller unit cell volume and density than calcite. Such a transformation has been shown to result in several micron thick voids within the spherulite core (Cherkas et al., 2017). There was no evidence of any voids, gaps, or displacement within the calcite spherulites (Figure 4C). The refined unit cell of the spherulitic calcite matches to low Mg^{2+} calcite (Antao and Hassan, 2010) (Figure 7). Calcite nanocrystals in the core are crystallographically aligned radially. There are two lines of evidence for this. First, diffraction peaks show a high degree of preferred orientation. Second, cross polarized microscopy studies of a bisected spherulite (half of a sphere in epoxy not thin section) yielded a Maltese cross pattern.

A Maltese cross will not be observed unless most or all of the crystallites in the spherulite are radially oriented crystallographically, i.e., pointing away from the center of the spherulite. Cross polarized microscopy also confirmed that the crystallites are elongated along the *c*-axis. In calcite the *c*-axis is also the optic axis. At the very center of the cross polarized microscopy spherulite in Figure 4E the crystallites are oriented away from the viewer, i.e., their axis of elongation is perpendicular to the stage. Because the axis of elongation is also along the optic *c*-axis, the center of the sample always stays white, never pink, even as the stage is rotated. Any axis oblique to the optic *c*-axis of calcite would change white to pink under cross polarized microscopy. The white center disappears and becomes a perfect X when switched to plain polarized light. The third line of evidence that the *c*-axis is the axis of elongation is the formation of the 3-armed crystals coating

outer spherulites (Figure 4D), these grew parallel to the fibers beneath. Since calcite only has one 3-fold axis, aka its *c*-axis, the 3-armed or 3-fold morphology (figure 1B) is evidence of being along it.

4.2.2 Struvite

SEM-EDS analyses of the transparent orthorhombic crystals yielded peaks of Mg ($K\alpha$ 1.253), O ($K\alpha$ 0.525), and P ($K\alpha$ 2.013). Light elements such as N and H are not detectable by EDS. Single crystal XRD yielded a refined unit cell of $a= 6.961$, $b= 6.150$, $c= 11.249$, which matched that of struvite.

4.2.3 Guanine Monohydrate

Orange globular opaque spherulites were soft and highly soluble so they were analyzed without cleaning. Under SEM-EDS analyses produced only one peak of C ($K\alpha$ 0.277). ToF-SIMS spectra matched guanine monohydrate ($C_5H_5N_5OH$), sodium guanine tetrad ($C_5H_5N_5ONa$), and potassium guanine tetrad ($C_5H_5N_5OK$) (Figure 8). The latter two were artefacts due to Na^+ and K^+ contamination in the sample. The fact that these are contamination artefacts was confirmed with Attenuated Total Reflection Fourier Transform Infrared (ATR-FTIR) spectroscopy on a sample that was pure and clean, obtained by cleaving a monocrystal. All spectra peaks matched guanine monohydrate (Figure 9). Biogenic guanine crystals in eukaryotes are nearly always anhydrous guanine ($C_5H_5N_5O$). In our sample, no anhydrous phase was detected. Despite the hexagonal morphology being indicative of the anhydrous guanine phase, ATR-FTIR of the hexagonal crystals in figure 5C also matched guanine monohydrate.

4.3 Identification of Bacteria

The nucleotide sequence of the near full-length 16S rRNA of the isolated bacterium matched that of *Pseudoaltermonas haloplanktis* with 99% similarity (Figure 10). This bacterium is common in saline marine environments at or near 70 °C (Michela Corsaro et al., 2001).

4.4 pH Increase

The pH increase in bacteria culture was shown both in experiments with liquid and solid Luria-Bertani media. In liquid culture, the pH of the medium was measured with a pH probe while the bacterial growth was monitored by measurement of culture optical density at 600 nm. On the first day, there was appreciable bacterial growth but no substantial change in culture pH. Thereafter, culture density and pH rose synonymously before plateauing. The final pH of the culture, when bacterial growth seized and became stationary, was 7.8 (Figure 3).

4.5 pH Tolerance

The above experiment showed that the culture stopped growing when the culture pH reached 7.8. I wondered whether or not the high pH was the cause of bacterial growth stoppage. To answer that question, I determined the bacterium's pH tolerance. I grew liquid cultures that were adjusted to various pH values and kept at the values with various buffers: pH 7, pH 8, pH9, pH 10, and pH 11. Bacterial growth was fastest at pH 8. No or little growth was observed at pH 10.5 (Figure 11). Therefore, the alkaline pH of 7.8 is not the reason why the bacteria stopped growing in unbuffered liquid LB experiment.

Chapter 5: Discussion

5.1 Overlap with Nature

In a bacterial culture, and in nature, sustained bacterial growth requires continuous access to nutrients and removal of metabolic wastes. In a well-mixed liquid culture, there are no gradients in the distribution of nutrients or wastes. All bacteria in it grow at the same rate. However, in this experiment with a solid medium, nutrients have to diffuse to the colony from the surrounding agar while metabolic wastes have to diffuse out of the colony to the surrounding agar. Both diffusion processes become increasingly more obstructed by bacteria and biofilm as the colony grows bigger. Hence the size of a bacterial colony grown on agar, apart from species that can swarm, is finite. This study shows that the same two diffusion processes also control the formation of calcite spherulite formations.

5.2 Effect of Carbohydrates

The precipitation of calcite on solid Luria-Bertani medium did not begin until the colony reached approximately 2 cm in diameter (Figure 4A). This may seem counterintuitive. The growth rate of a colony is highest in the beginning. In other words, throughout the media fueled growth of a colony, activity only decreases, never increases. The delay in spherulite formation is attributed to the fact that Luria-Bertani medium contains approximately 4% carbohydrates (BD DIFCO™ LB Broth, SKU: 240230). Consequently, as long as bacteria are consuming carbohydrates, the colony puts out CO₂, but not NH₃. Without NH₃, alkalinity will not rise (Figure 3). Indeed, when I grew the bacterium in a defined medium composed of no carbohydrates and only amino acids (10.0g/L glutamic acid) spherulite formation began immediately, forming large crystals visible to the naked

eye by day two.

5.3 Spherulite Formation on Colonies

The process of nucleating a new crystal vs continued growth of an existing crystal are energetically different physicochemical processes. Nucleation of calcite is a multi-step exothermic process, consisting of aggregation of hydrous amorphous calcium carbonate (ACC) clusters, dehydration of ACC clusters, crystallization of metastable phases, and Ostwald ripening into stable nanocrystalline calcite seeds (Cartwright et al., 2012). The continued growth of an existing crystal is a one step process, through straightforward addition of ions from solution to crystal surface defects. Hence, nucleation requires more energy or higher levels of alkalinity than continued crystal growth. Hence, in a diffusion free system, there can only be a single nucleation event, after which no new crystals form. All available calcium and alkalinity would go into the growth of existing crystals, preventing saturation from ever rising over the nucleation energy barrier. The situation is different in a colony grown on an agar medium, however. The colony, comprised of bacteria and biofilm, is a large diffusion barrier, especially as the colony grows bigger, thereby to some extent trapping the NH_3 and CO_2 metabolic wastes. In other words, NH_3 is highest in the center of the colony and decreases as a function of distance from it to the surrounding medium (NH_3 was confirmed with a Hach Ammonia Test Kit). This creates a gradient in pH (Figure 12). Calcium is homogenously distributed in the agar plate because bacteria do not metabolize it. Additionally, atmospheric CO_2 is readily available. When colonies are intentionally inoculated such that spacing between them is minimal throughout the plate, spherulites precipitated in agar as well, thereby without bacteriogenic CO_2 . This means that CaCO_3 saturation is controlled by the distribution of NH_3 , not Ca or CO_2 . Specifically, CaCO_3 saturation is reached 2-5 mm inside the

colony edge, where the gradient of NH_3 diffusing out meets Ca^{2+} diffusing in. For a period after spherulites appeared, existing spherulites inhibited new spherulites from being nucleated, even though the colony grew in size. This is because the growth of existing spherulites depletes calcium and lowers the saturation level of its surroundings, preventing alkalinity from rising above the nucleation barrier, thus inhibiting nucleation. This inhibitive condition disappears, and new spherulites are nucleated once the buildup of alkalinity between the previous row and the colony edge overcomes the nucleation energy barrier. Once a new row of spherulites is formed, calcium diffusing in from the surrounding agar is intercepted, and the older row to their inside is deprived and stops growing. With each new row, the size of individual spherulites increases while the quantity of spherulites nucleated decreases. Furthermore, the band of bacteria separating existing spherulites from fresh agar becomes wider. These trends are due to the fact that the rate of NH_3 output in the colony decreases as the colony becomes larger, a result of bacterial inaccessibility to nutrients with further colony growth. This alternating cycle between growth of existing spherulites and the nucleation of new spherulites continues until colony growth comes to a stop.

5.4 PO_4^{3-} Induced Stoppage

The growth of spherulites has been terminated when new spherulites appeared to their outside. The outermost row of spherulites temporarily paused their growth before this happened: due to a rise of phosphate, which is known to inhibit the precipitation of CaCO_3 (Figure 4C) (Schlesinger & Hay, 1986 ; Burton' and Walters, 1990). This sudden rise in phosphate in the colony's environment could only come from the degradation of dead cells in the colony center. As the colony grows larger, only the edge is growing, where there is access to nutrients from the surrounding agar. Cells

in the center of the colony are starved of nutrients, die, and are recycled as a source of carbon (Figure 13B). The arrested growth of the last row of spherulites suggests that by this point in time, the degradation process has proceeded to the point that phosphate-containing macromolecules, including DNA and phospholipids, had been degraded. After a pause, calcite spherulite growth resumed. This is the result of struvite precipitation. The solubility of struvite decreases with increasing pH and precipitates at near neutral pH in the presence of NH_3 . A sudden infusion of phosphate into an alkaline environment with high levels of NH_3 and Mg^{2+} induced rapid precipitation of struvite, thereby depleting PO_4^{3-} and releasing spherulites from inhibition. The fact that the resumed spherulite growth continued to be nanocrystalline suggests that the colony edge was still metabolically active at this point. The texture of spherulite growth soon became micro-prismatic (after $\sim 20 \mu\text{m}$ of growth) (Figure 4C), suggesting that the activity of the colony began to slow down considerably and was not far from the end of its life. On plates where a larger number of colonies grew close to one another such that higher levels of alkalinity could be generated, another row of spherulites were initiated at this time. These spherulites stopped growing at a very small size, again confirming that the colony was approaching the end of its life at that point.

5.5 Three-fold Layer on Spherulites

The end of colony growth and activity coincides with the formation of a thin covering of 3-fold calcite superstructures on the last row of spherulites, each $15 \mu\text{m}$ from tip to tip (fig 1B). At this point, NH_3 and CO_2 production by bacteria is at too low a rate to substantially overcome diffusion and accumulate in the colony, resulting in low supersaturation. The formation of 3-fold calcite requires two conditions: low supersaturation with respect to CaCO_3 and presence of short peptides.

The same 3-fold unit, but much smaller in size (< 500 nm), on average 1-10 nm, is a rough final coating on the platelets of nacre (gastropods and bivalves), shell of the giant barnacle *Austromegabalanus psittacus*, tips of spherulites in *Nautilus macromphalus*, and even vertebrates such as fish otoliths and avian eggshells (Checa et al., 2020). In these examples, the same biomolecules previously controlling crystal growth instead induce a 3-fold structure at the end of biomineralization, when saturation conditions are much lower. The size difference between the 3-fold examples in nature and those in this study is due to these transient low saturation conditions being extended by bacteria with month long cellular recycling continuously producing scant NH_3 . 3-fold growth requiring low supersaturation as well as a peptide was confirmed in a clean laboratory synthesis experiment using sericin, a 4 amino acids long peptide extracted from nacre (Pastero and Aquilano, 2018). The exact molecular interactions between sericin and calcite that led to the face-specific inhibition have yet to be defined through lattice matching. In the sericin experiment, the 3-fold morphology only resulted when growth rate of calcite was near the adsorption rate of sericin onto calcite, this was achieved only when running the experiment at low supersaturating conditions. Under these conditions, the three $\{104\}$ rhombohedral faces continued growth particularly in the $\langle \bar{4}41 \rangle$ directions while the remaining planes perpendicular to c , especially along $\{110\}$ were inhibited. The same crystallographic growth bias is seen in all of the known examples in nature, and the 3-fold coating on the spherulites in this study (Figure 1C). The ability of organic molecules to adsorb onto planes perpendicular to calcite's c -axis decreases with increased lattice bond strength, which varies in crystallographic direction. Thus, the periodic bond chains (PBC's) of calcite, $\langle 010 \rangle$, $\langle 42\bar{1} \rangle$, and $\langle \bar{4}41 \rangle$ are resistant to adsorption. The $\langle \bar{4}41 \rangle$ directions are by far the strongest, hence biomolecules are hardly incorporated along $\langle \bar{4}41 \rangle$, rather

expelled sideways during growth (Figures 1B and 1C) (Aquilano et al., 2011; Checa et al., 2020). Short peptides, either four or five amino acids long, are known components of peptidoglycans, a structural polymer that form the cell wall of bacteria. Peptidoglycans are highly recalcitrant. They are one of the last polymers in dead bacteria to be degraded. In this study, by the time the thin layer made of 3-fold calcite monocrystals began to form, guanine monohydrate crystals formed on top of the colony, suggesting that DNA was already degraded (Fig. 7 B). It is likely that by this time peptidoglycans were depolymerized as well, but only the sugar backbone was degraded, leaving the cross-linking peptides intact to induce the formation of the 3-fold calcite unit in the low supersaturation conditions.

Chapter 6: Relevance to Nature Discussion

6.1 Spherulites in Mollusks

Calcium carbonate spherulites like those in this experiment are synthesized by mollusks, under certain circumstances, as parts of their shells. Typically, the CaCO_3 components of a mollusk shell, which is protected from dissolution by an organic layer of scleroprotein or chitin, called the periostracum, is divided into two layers: a prismatic layer, that typically consists of calcite crystals (10-40 μm long and 0.5-3 μm thick) hexagonal in cross section and elongated about their *c*-axis, and a nacreous layer that is comprised of flat aragonite platelets (10–20 μm wide and ~0.5 μm thick) cemented together by elastic biopolymers. The growth of both layers is under highly sophisticated control using biomineralizing proteins and slow growth. There are scenarios where these animals need to relax their control to allow CaCO_3 to precipitate in the more primitive spherulitic growth form. These scenarios all include a need for rapid growth: Warm summer months when shell growth is rapid in which case spherulites are precipitated in between the periostracum and prismatic layer (Nishida et al., 2011), initial stages of pearl and shell blister growth to entomb intruding parasites or debris (Hänni, 2012), and during the repair of shell fracture (Fleury et al., 2008). Thus, the evolution of mollusks is not a process where primitive biomineralization controls are discarded as more sophisticated controls are invented. Rather, the primitive controls are retained. In other words, they possess an expanded repertoire of controls that include the primitive as well as the advanced. The primitive spherulitic growth form still useful for rapid biomineralizing scenarios.

6.2 Spherulites in Stromatolites

Carbonate spherulites also make up stromatolites, layered organo-sedimentary structures that formed on Earth from the Eoarchean Era, 3.5 billion years ago, to today. Today, stromatolites are associated with cyanobacteria-dominated microbial mats, notably, those in Shark Bay Australia. The role of cyanobacteria is well known. Cyanobacteria possess an extracellular polysaccharide sheath, which is negatively charged and absorbs divalent ions including calcium. During the day, they photosynthesize, taking up CO_2 and bicarbonate, thereby causing the pH of the interstitial water to increase. Such water is undersaturated, not oversaturated, with respect to CaCO_3 , however. If anything, this water facilitates CaCO_3 dissolution. If precipitation does occur during this time, atmospheric CO_2 would cause CaCO_3 precipitates be enriched in inorganic ^{13}C . It has been found that carbonate in stromatolites is enriched in ^{12}C , however (Andres et al., 2006). Thus, CaCO_3 precipitation occurs in the mat only at night when cyanobacteria CO_2 fixation ceases and heterotrophic bacterial processes release NH_3 and CO_2 , due to degradation of buried organics, which diffuse upwards into the Ca-enriched interstitial water in the polysaccharide matrix. This would suggest that heterotrophic bacteria like those in this study, are the real stromatolite builders. This study demonstrates that bacterial activity rate dictates how far into the biofilm Ca^{2+} travels before precipitation occurs. Extending this finding into a natural stromatolite system, the heterotrophic bacterial activity rate can be approximated based on the thickness of the biofilm separating the hypersaline water from the mineral surface, as CO_2 is the limiting reactant in this precipitation system. This can also be used to quickly monitor stromatolite growth rate, a topic of much interest due to unease about climate change impacts to stromatolite formation. Additionally, this study adds to the growing body of evidence that the spherulite formations in stromatolites are

morphologically the result of proteins, peptides, and amino acids inevitably present in a microbial mat.

6.3 Struvite and Calcite in the Urinary Tract

Urolithiasis, a medical condition due to the formation of stone obstructions, when bacteria cause urinary tract infections (UTI). Urea ($\text{CO}(\text{NH}_2)_2$) is an energy source for bacteria. Like the bacterial oxidation of amino acids, when bacteria cleave urea, they produce NH_3 and CO_2 waste products. NH_3 combines with Mg^{2+} and PO_4^{3-} in urine forming struvite, even at neutral pH conditions. Advances in spectroscopy have led to the discovery of calcite spherulites in the urine of patients with a UTI (Frochot et al., 2021). This suggests that presence of calcite in urine could be a diagnostic of struvite urolithiasis. Why struvite urolithiasis is accompanied by CaCO_3 precipitation is poorly understood. The traditional explanation is due to high urinary pH as a result of NH_3 production by bacteria. A more likely non-exclusive answer is that free phosphate, which is ordinarily present in urine at high enough levels to inhibit CaCO_3 precipitation, is sequestered by the precipitation of struvite. As experiments in this study show, calcite spherulite precipitation continues until bacterial release of phosphate inhibited it, only resuming once struvite formed. Indeed, rat mutants lacking the gene responsible for urinary acidification, have high urinary pH, without UTI's, i.e., no NH_3 , developed calcium phosphate urolithiasis (Wagner and Mohebbi, 2010). In another rat experiment, PO_4^{3-} concentration in urine was deliberately lowered by feeding the animal a high calcium diet, a process that precipitates calcium phosphate in the gastrointestinal tract, thus lowering excreted PO_4^{3-} in urine, and forming CaCO_3 spherulites in the rat's urine at healthy urinary pH (Takeuchi et al., 1991). Thus, in mammals, the excretion of NH_3 and CO_2

wastes in the form of urea ($\text{CO}(\text{NH}_2)_2$) is a remarkable biomineral prevention strategy. As UTI's demonstrate, even at healthy pH levels, presence of NH_3 induces struvite stone formation, sequestering PO_4^{3-} and removing our defense against CaCO_3 precipitation.

References

- Albeck, S., Aizenberg, J., Addadi, L., and Weiner, S., 1993, Interactions of Various Skeletal Intracrystalline Components with Calcite Crystals: *Journal of the American Chemical Society*, v. 115, p. 11691–11697, doi:10.1021/ja00078a005.
- Andres, M.S., Sumner, D.Y., Reid, R.P., and Swart, P.K., 2006, Isotopic fingerprints of microbial respiration in aragonite from Bahamian stromatolites: *Geology*, v. 34, p. 973–976, doi:10.1130/G22859A.1.
- Aquilano, D., Bruno, M., Massaro, F.R., and Rubbo, M., 2011, Theoretical equilibrium shape of calcite. 2. [441] zone and its role in biomineralization: *Crystal Growth and Design*, v. 11, p. 3985–3993, doi:10.1021/cg2005584.
- Antao, S.M., and Hassan, I., 2010, Temperature dependence of the structural parameters in the transformation of aragonite to calcite, as determined from in situ synchrotron powder X-ray-diffraction data: *Canadian Mineralogist*, v. 48, p. 1225–1236, doi:10.3749/canmin.48.5.1225.
- Braissant, O., Cailleau, G., Dupraz, C., and Verrecchia, E.P., 2003, Bacterially induced mineralization of calcium carbonate in terrestrial environments: The role of exopolysaccharides and amino acids: *Journal of Sedimentary Research*, v. 73, p. 485–490, doi:10.1306/111302730485.
- Englert, K.M., McAteer, J.A., Lingeman, J.E., and Williams, J.C., 2013, High carbonate level of apatite in kidney stones implies infection, but is it predictive: *Urological Research*, v. 41, p. 389–394, doi:10.1007/s00240-013-0591-6.
- Frochot, V., Castiglione, V., Lucas, I.T., Haymann, J.P., Letavernier, E., Bazin, D., Fogazzi, G.B., and Daudon, M., 2021, Advances in the identification of calcium carbonate urinary crystals: *Clinica Chimica Acta*, v. 515, p. 1–4, doi:10.1016/j.cca.2020.12.024.
- Burton, E.A., and Walters, L.M., 1990, The role of pH in phosphate inhibition of calcite and aragonite precipitation rates in seawater.:
- Cartwright, J.H.E., Checa, A.G., Gale, J.D., Gebauer, D., and Sainz-Díaz, C.I., 2012, Calcium carbonate polyamorphism and its role in biomineralization: How many amorphous calcium carbonates are there? *Angewandte Chemie - International Edition*, v. 51, p. 11960–11970, doi:10.1002/anie.201203125.
- Checa, A.G., Macías-Sánchez, E., Rodríguez-Navarro, A.B., Sánchez-Navas, A., and Lagos, N.A., 2020, Origin of the biphasic nature and surface roughness of biogenic calcite secreted by the giant barnacle *Austromegabalanus psittacus*: *Scientific Reports*, v. 10, doi:10.1038/s41598-020-73804-8.

- Cherkas, O., Beuquier, T., Breiby, D.W., Chushkin, Y., Zontone, F., and Gibaud, A., 2017, Direct Observation of Microparticle Porosity Changes in Solid-State Vaterite to Calcite Transformation by Coherent X-ray Diffraction Imaging: *Crystal Growth and Design*, v. 17, p. 4183–4188, doi:10.1021/acs.cgd.7b00476.
- Christy, A.G., 2017, A Review of the Structures of Vaterite: The Impossible, the Possible, and the Likely: *Crystal Growth and Design*, v. 17, p. 3567–3578, doi:10.1021/acs.cgd.7b00481.
- Dominguez Bella, S., and Garcia-Ruiz, J.M., 1986, Textures in induced morphology crystal aggregates of CaCO₃: Sheaf of wheat morphologies: *Journal of Crystal Growth*, v. 79, p. 236–240, doi:10.1016/0022-0248(86)90444-6.
- Eder, W., Ludwig, W., and Huber, R., 1999, Novel 16S rRNA gene sequences retrieved from highly saline brine sediments of Kebrit Deep, Red Sea: *Archives of Microbiology*, v. 172, p. 213–218, doi:10.1007/s002030050762.
- Felsenstein, J., 1985, Confidence Limits on Phylogenies: An Approach Using the Bootstrap: *Evolution*, v. 39, p. 783, doi:10.2307/2408678.
- Fleury, C., Marin, F., Marie, B., Luquet, G., Thomas, J., Josse, C., Serpentine, A., and Lebel, J.M., 2008, Shell repair process in the green ormer *Haliotis tuberculata*: A histological and microstructural study: *Tissue and Cell*, v. 40, p. 207–218, doi:10.1016/j.tice.2007.12.002.
- Granasy, L., Pusztai, T., and Borzsonyi, T., 2007, Phase Field Theory of Nucleation and Polycrystalline Pattern Formation: , p. 1–48, <http://arxiv.org/abs/cond-mat/0703676>.
- Hänni, H., 2012, Natural pearls and cultured pearls: A basic concept and its variations.:
- Kai, A., Fujikawa, K., and Miki, T., 2002, Vaterite stabilization in CaCO₃ crystal growth by amino acid: *Japanese Journal of Applied Physics, Part 1: Regular Papers and Short Notes and Review Papers*, v. 41, p. 439–444, doi:10.1143/JJAP.41.439.
- Konopacka-Łyskawa, D., Kościelska, B., and Łapiński, M., 2019, Precipitation of Spherical Vaterite Particles via Carbonation Route in the Bubble Column and the Gas-Lift Reactor: *Jom*, v. 71, p. 1041–1048, doi:10.1007/s11837-018-3307-0.
- Kumar, S., Mitnik, C., Valente, G., and Floyd-Smith, G., 2000, Expansion and molecular evolution of the interferon-induced 2'-5' oligoadenylate synthetase gene family: *Molecular Biology and Evolution*, v. 17, p. 738–750, doi:10.1093/oxfordjournals.molbev.a026352.
- Liu, D., and Yates, M.Z., 2006, Formation of rod-shaped calcite crystals by microemulsion-based synthesis: *Langmuir*, v. 22, p. 5566–5569, doi:10.1021/la060612i.
- Mann, S., Didymus, J.M., Sanderson, N.P., Heywood, B.R., and Samper, E.J.A., 1990, Morphological influence of functionalized and non-functionalized α,ω -dicarboxylates on

- calcite crystallization: *Journal of the Chemical Society, Faraday Transactions*, v. 86, p. 1873–1880, doi:10.1039/FT9908601873.
- Marangoni, A.G., and Ollivon, M., 2007, Fractal character of triglyceride spherulites is a consequence of nucleation kinetics: *Chemical Physics Letters*, v. 442, p. 360–364, doi:10.1016/j.cplett.2007.05.098.
- McGinnis, S., and Madden, T.L., 2004, BLAST: At the core of a powerful and diverse set of sequence analysis tools: *Nucleic Acids Research*, v. 32, p. 20–25, doi:10.1093/nar/gkh435.
- Michela Corsaro, M., Lanzetta, R., Parrilli, E., Parrilli, M., and Luisa Tutino, M., 2001, Structural investigation on the lipooligosaccharide fraction of psychrophilic pseudoalteromonas haloplanktis TAC 125 bacterium: *European Journal of Biochemistry*, v. 268, p. 5092–5097, doi:10.1046/j.0014-2956.2001.02429.x.
- Nath, K., and Koch, A.L., 1970, Protein Degradation in *Escherichia coli*: *Journal of Biological Chemistry*, v. 245, p. 2889–2900, doi:10.1016/s0021-9258(18)63072-8.
- Nishida, K., Nakashima, R., Majima, R., and Hikida, Y., 2011, Ontogenetic changes in shell microstructures in the cold seep-associated bivalve, *conchocele bisecta* (Bivalvia: Thyasiridae): *Paleontological Research*, v. 15, p. 193–212, doi:10.2517/1342-8144-15.4.193.
- Pastero, L., and Aquilano, D., 2018, Calcium carbonate polymorphs growing in the presence of sericin: A new composite mimicking the hierarchic structure of Nacre: *Crystals*, v. 8, doi:10.3390/cryst8070263.
- Pokroy, B., Kabalah-Amitai, L., Polishchuk, I., Devol, R.T., Blonsky, A.Z., Sun, C.Y., Marcus, M.A., Scholl, A., and Gilbert, P.U.P.A., 2015, Narrowly Distributed Crystal Orientation in Biomineral Vaterite: *Chemistry of Materials*, v. 27, p. 6516–6523, doi:10.1021/acs.chemmater.5b01542.
- Porter, K.G., Feig, Y.S., Sep, N., Jannasch, H.W., Zafiriou, O.C., and Farrington, J.W., 2007, The Use of DAPI for Identifying and Counting Aquatic Microflora The use of DAPI for identifying and counting aquatic microfloral: *Limnology*, v. 25, p. 943–948.
- Prescher, C., and Prakapenka, V.B., 2015, DIOPTAS: A program for reduction of two-dimensional X-ray diffraction data and data exploration: *High Pressure Research*, v. 35, p. 223–230, doi:10.1080/08957959.2015.1059835.
- Pusztai, T., Tegze, G., Tóth, G.I., Környei, L., Bansel, G., Fan, Z., and Grínsy, L., 2008, Phase-field approach to polycrystalline solidification including heterogeneous and homogeneous nucleation: *Journal of Physics Condensed Matter*, v. 20, doi:10.1088/0953-8984/20/40/404205.

- Qiao, L., and Feng, Q.L., 2007, Study on twin stacking faults in vaterite tablets of freshwater lacklustre pearls: *Journal of Crystal Growth*, v. 304, p. 253–256, doi:10.1016/j.jcrysgro.2007.02.001.
- Rodriguez-Navarro, C., Jimenez-Lopez, C., Rodriguez-Navarro, A., Gonzalez-Muñoz, M.T., and Rodriguez-Gallego, M., 2007, Bacterially mediated mineralization of vaterite: *Geochimica et Cosmochimica Acta*, v. 71, p. 1197–1213, doi:10.1016/j.gca.2006.11.031.
- Saitou, N., and Nei, M., 1987, The neighbor-joining method: a new method for reconstructing phylogenetic trees.: *Molecular biology and evolution*, v. 4, p. 406–425, doi:10.1093/oxfordjournals.molbev.a040454.
- Sánchez-Román, M., Romanek, C.S., Fernández-Remolar, D.C., Sánchez-Navas, A., McKenzie, J.A., Pibernat, R.A., and Vasconcelos, C., 2011, Aerobic biomineralization of Mg-rich carbonates: Implications for natural environments: *Chemical Geology*, v. 281, p. 143–150, doi:10.1016/j.chemgeo.2010.11.020.
- SCHLESINGER, D.H., and HAY, D.I., 1986, Complete covalent structure of a proline-rich phosphoprotein, PRP-2, an inhibitor of calcium phosphate crystal growth from human parotid saliva: *International Journal of Peptide and Protein Research*, v. 27, p. 373–379, doi:10.1111/j.1399-3011.1986.tb01030.x.
- Takeuchi, H., Ueda, M., Satoh, M., and Yoshida, O., 1991, Effects of dietary calcium, magnesium and phosphorus on the formation of struvite stones in the urinary tract of rats.:
- Tamura, K., Dudley, J., Nei, M., and Kumar, S., 2007, MEGA4: Molecular Evolutionary Genetics Analysis (MEGA) software version 4.0: *Molecular Biology and Evolution*, v. 24, p. 1596–1599, doi:10.1093/molbev/msm092.
- Tamura, K., Stecher, G., and Kumar, S., 2021, MEGA11: Molecular Evolutionary Genetics Analysis Version 11: *Molecular Biology and Evolution*, v. 38, p. 3022–3027, doi:10.1093/molbev/msab120.
- Toby, B.H., and von Dreele, R.B., 2013, GSAS-II: The genesis of a modern open-source all purpose crystallography software package: *Journal of Applied Crystallography*, v. 46, p. 544–549, doi:10.1107/S0021889813003531.
- Wagner, C.A., and Mohebbi, N., 2010, Urinary pH and stone formation: *Journal of Nephrology*, v. 23.
- Zhao, Y., Han, Z., Yan, H., Zhao, H., Tucker, M.E., Gao, X., Guo, N., Meng, R., and Owusu, D.C., 2021, Selective Adsorption of Amino Acids in Crystals of Monohydrocalcite Induced by the Facultative Anaerobic Enterobacter ludwigii SYB1: *Frontiers in Microbiology*, v. 12, p. 1–17, doi:10.3389/fmicb.2021.696557.

Zhou, Z.Y., Tian, N., Li, J.T., Broadwell, I., and Sun, S.G., 2011, Nanomaterials of high surface energy with exceptional properties in catalysis and energy storage: *Chemical Society Reviews*, v. 40, p. 4167–4185, doi:10.1039/c0cs00176g.

Curriculum Vitae

Zakaria Jibrin
zakjibrin@gmail.com

EDUCATION

- **Bachelor of Science: Geology con. mineralogy, University of Arizona 2015-2019**
- **Master of Science: Geosciences, thesis: Biomineralogy, University of Nevada, Las Vegas, 2019 - 2022**

RESEARCH EXPERIENCE

Research assistant, Desert Research Institute, May 2019 – Nov 2022

- Conducted self-appointed research on biomineralization of calcite spherulites, struvite, and guanine monohydrate by halophilic bacteria from Death Valley CA.
- Analyzed nanocrystals through the use of the Lawrence Berkely's synchrotron beamline 12.3.2
- Identified implications for biominerals in kidney stone formation
- Progressed understanding of how bacterial cultures induce a mineral forming environment and how they influence crystal structure/growth

Lab technician, RRUFF laboratory University of Arizona, January 2017- May 2019

- Analyzed and performed data analysis on samples using powder and single crystal X-Ray Diffraction
- Polished and analyzed samples with Electron Microprobe or SEM EDS for chemical composition resolution
- Used Raman Spectrometer to rapidly identify samples and build database with the resulting spectra

ANALYTICAL EQUIPMENT

- Synchrotron X-ray Microdiffraction
- Single crystal X-ray Diffraction
- Powder X-ray Diffraction
- Scanning Electron Microscope
- Raman Spectroscopy
- Field Emission Scanning Electron Microscope
- Electron Microprobe
- Mass spectrometry
- PCR and associated for 16S ribosomal RNA (rRNA) gene sequencing
- FTIR

DATA PROCESSING TOOLS

- Topas, Powder Cell, Dioptas, Jade, Adobe Photoshop, Adobe Illustrator, Microsoft Office Suite, ArcGIS Pro, Mega X

AWARDS/ACCOMPLISHMENTS

- Co-authored in papers involving the discovery of lazaraskeite, liudongshengite, and magnesioalterite
- David L. Moore Memorial Scholarship, Arizona Award of Excellence Scholarship
- Published mineral photography for a publication of Mineralogical Record (Mexico)